

Article pubs.acs.org/iournal/abseba

Biogenesis of Extracellular Vesicles Produced from Human-Stem-Cell-Derived Cortical Spheroids Exposed to Iron Oxides

Mark Marzano, Mayassa J. Bou-Dargham, Allaura S. Cone, Sara York, Shannon Helsper, Samuel C. Grant, David G. Meckes, Jr., Qing-Xiang Amy Sang, and Yan Li*



Cite This: ACS Biomater. Sci. Eng. 2021, 7, 1111-1122



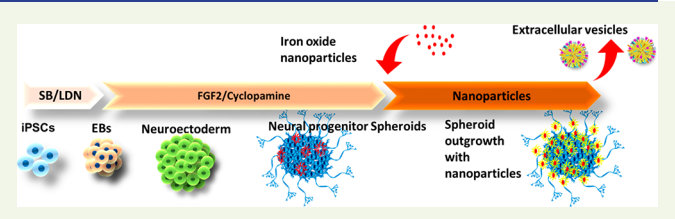
ACCESS I

Metrics & More

Article Recommendations

Supporting Information

ABSTRACT: Stem-cell-derived extracellular vesicles (EVs) are promising tools for therapeutic delivery and imaging in the medical research fields. EVs that arise from endosomal compartments or plasma membrane budding consist of exosomes and microvesicles, which range between 30 and 200 nm and 100-1000 nm, respectively. Iron oxide nanoparticles can be used to label stem cells or possibly EVs for magnetic resonance imaging. This could



be a novel way to visualize areas in the body that are affected by neurological disorders such as stroke. Human induced pluripotent stem cells (iPSK3 cells) were plated on low-attachment plates and treated with SB431542 and LDN193189 during the first week for the induction of cortical spheroid formation and grown with fibroblast growth factor 2 and cyclopamine during the second week for the neural progenitor cell (iNPC) differentiation. iNPCs were then grown on attachment plates and treated with iron oxide (Fe₃O₄) nanoparticles at different sizes (8, 15, and 30 nm in diameter) and concentrations (0.1, 10, and 100 μ M). The spheroids and media collected from these cultures were used for iron oxide detection as well as EV isolation and characterizations, respectively. MTT assay demonstrated that the increased size and concentration of the iron oxide nanoparticles had little effect on the metabolic activity of iNPCs. In addition, the Live/Dead assay showed high viability in all the nanoparticle treated groups and the untreated control. The EVs isolated from these culture groups were analyzed and displayed similar or higher EV counts compared with control. The observed EV size averaged 200-250 nm, and electron microscopy revealed the expected exosome morphology for EVs from all groups. RT-PCR analysis of EV biogenesis markers (CD63, CD81, Alix, TSG101, Syntenin1, ADAM10, RAB27b, and Syndecan) showed differential expression between the iron-oxide-treated cultures and nontreated cultures, as well as between adherent and nonadherent 3D cultures. Iron oxide nanoparticles were detected inside the cortical spheroid cells but not EVs by MRI. The addition of iron oxide nanoparticles does not induce significant cytotoxic effects to cortical spheroids. In addition,, nanoparticles may stimulate the biogenesis of EVs when added to cortical spheroids in vitro.

KEYWORDS: extracellular vesicles, exosomes, cortical spheroids, iron oxide nanoparticles, biogenesis, human induced pluripotent stem cells

1. INTRODUCTION

Stem-cell-derived extracellular vesicles (EVs) have attracted growing interest recently because of the therapeutic effects that are mainly attributed to the stem cell secretome. 1-4 EVs arise from plasma membrane budding, endosomal compartments, or as a result of apoptosis and consist of microvesicles, exosomes, and apoptotic bodies. Microvesicles and exosomes range from anywhere between 100 and 1000 nm and 30-200 nm, respectively.⁵ In particular, induced pluripotent stem cell (iPSC)-derived EVs have shown therapeutic effects in treating heart diseases, 3,6-8 stroke, 9,10 liver fibrosis, 11 aging, 12 high glucose induced injury, 13 and skin regeneration. 14 For therapeutic purposes, iPSC-EVs are considered safer than the cells because there is no risk of teratoma formation associated with their usage.³ In addition to therapeutics, EVs have been used to model the diseases and reveal the pathological progression mechanism.15

The stem cell microenvironment can affect the cargo and biological properties of EVs. For example, the 3D micro-

environment (e.g., cancer organoids) has been reported to promote the HSP90 and EpCAM (the markers indicating cancer stem cell phenotype) expression in the secreted EVs compared to 2D culture, 16 better recapitulating the cargo of in vivo exosomes.¹⁷ Our previous studies also reveal that EVs released from 2D or 3D differentiated human iPSCs reflect developmental stages, tissue homeostasis, and lineage specification of the cells. 4,18 The functional EV properties are indicated by their differential abilities to increase cell viability, reduce oxidative stress, and promote neurogenesis. 18 In particular, recent brain organoid technology based on human iPSCs has provided a promising platform for studying cell-cell

Received: August 31, 2020 Accepted: January 25, 2021 Published: February 1, 2021





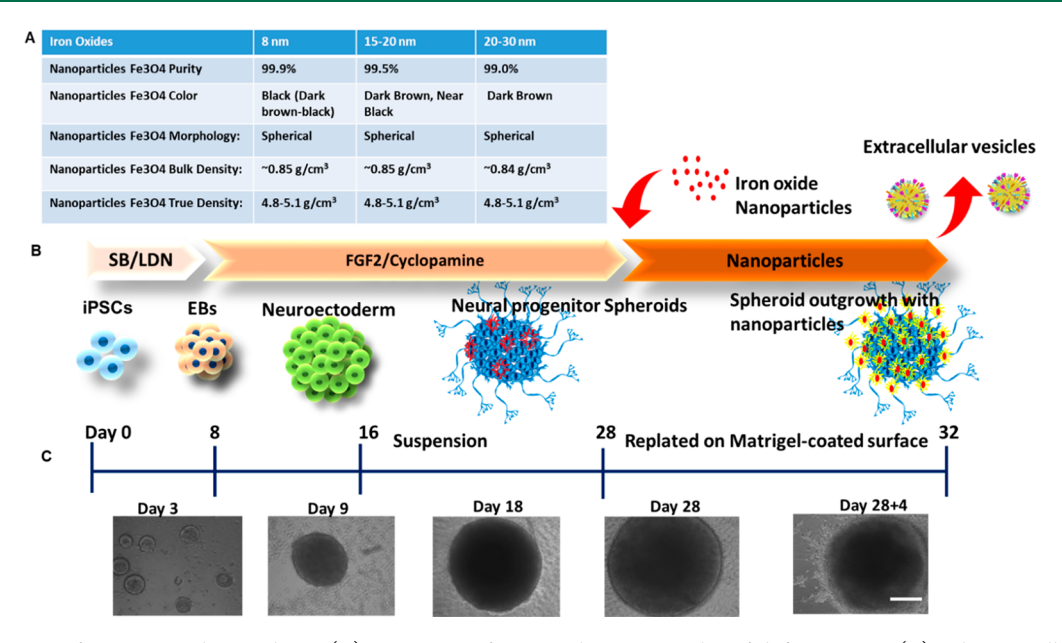


Figure 1. Illustration of experimental procedures. (A) Properties of iron oxide nanoparticles of different sizes. (B) Schematic illustration of the generation of cortical spheroids from human induced pluripotent stem cells and the addition of iron oxides. (C) Morphology of cortical spheroids at different time points of differentiation. Scale bar: $200 \ \mu m$.

communications and paracrine signaling in the human brain. $^{19-23}$

To understand the regeneration mechanisms due to stemcell-derived EVs, in vivo imaging such as magnetic resonance imaging (MRI) can be used to track EVs and ensure that they are able to reach target sites in the body and be retained within the tissue. To track EVs in vivo, we fabricated different types of nanoparticles (5-20 nm) to label the EVs, such as glucosecoated gold nanoparticles, 24,25 lectin-nanoparticles, 26 and ultrasmall superparamagnetic iron oxides (USPIOs).²⁷ Iron oxide nanoparticles recently have gained interest because they can be used to label EVs for in vivo tracking by MRI. 27,28 To enhance therapeutic effects of the EVs in animal studies, we evaluated EV encapsulation in polymer hydrogels (e.g., chitosan and collagen I). 29,30 It was found that incorporating EVs into thermosensitive chitosan hydrogels can improve EV stability, release, and retention in vitro, 29,30 as EVs can bind and become associated with extracellular matrices (ECM), whereas chitosan hydrogels can provide niche mimicking natural ECM. 31,32 However, questions remain as to how the culture microenvironment may affect EV biogenesis.

Taking one step further from our previous work, 18 the purpose of this study is to test the effects of iron oxide nanoparticles (with different sizes and concentrations) on the cortical spheroids differentiated from human iPSCs. More specifically, this study tested whether nanoscale iron oxides are toxic to cells from cortical spheroids and if they are involved in the EV biogenesis pathways. Our hypothesis is that nanoscale iron oxides at moderate concentrations do not affect the viability or metabolic activity of cortical spheroids. Furthermore, this study investigated if the nanoscale iron oxides can be detected within the EVs isolated from the culture medium of iron-oxide-labeled cortical spheroids. This study has implications for stem cell labeling by iron oxides, as well as revealing the effect of iron oxide labeling on EV biogenesis. This study is important for stem-cell-derived EV therapy in neurological disorders such as stroke and spinal cord injury.

2. MATERIALS AND METHODS

2.1. Preparation of Iron Oxide Nanoparticles. High-purity Fe_3O_4 magnetite nanoparticles were obtained from US Research Nanomaterials, Inc. (Houston, TX) of sizes 8 nm (stock no. US3208), 15-20 nm (stock no. US3230), and 20-30 nm (stock no. US3220) (Figure 1A). A stock solution of 10 mM per nanoparticles sizes was prepared by dispersing the nanoparticles in ultrapure water. The stock solutions were exposed to ultraviolet radiation overnight to sterilize the solution. Then the stocks were sonicated in a water bath sonicator at 4 °C for 20 min. Three dilutions were prepared by doing a serial dilution of the original stock in Dulbecco's Modified Eagle Medium (DMEM) plus 2% B27 and antibiotics. The final concentrations were 0.1 μ M (0.23 μ g Fe/mL), 10μ M (2.34 μ g Fe/mL), and 100μ M (23.4 μ g Fe/mL) for each nanoparticle size used. The samples were vortexed during the dilution procedure for a consistent preparation.

2.2. Differentiation of iPSK3 into Cortical Spheroids. Undifferentiated human iPSK3 cells were seeded into ultra-low attachment (ULA) 24-well plates (Corning Inc., Corning, NY) at 3 × 10⁵ cells/well in differentiation medium composed of DMEM/F-12 plus 2% B27 serum-free supplement (Life Technologies, Carlsbad, CA). iPSK3 cells were seeded in the presence of Y27632 (10 μ M). After 24 h, Y27632 was removed and the formed embryoid bodies (EB) were treated with dual SMAD signaling inhibitors of 10 μ M SB431542 (Sigma-Aldrich, St. Louis, MO) and 100 nM LDN193189 (Sigma) over 7 days. Then on day 8, the spheroids were treated with fibroblast growth factor (FGF)-2 (10 ng/mL, Life Technologies) and cyclopamine (an Shh inhibitor, 1 µM, Sigma) for cortical differentiation for 21 days. 22,33,34 The cells were replated onto growth factor reduced Matrigel-coated surfaces and treated with different iron oxide nanoparticles for another 2-4 days prior to further downstream experiments (Figure 1B, C). On the basis of our previous studies, 35,36 the labeling efficiency for microsized particles of iron oxides (MPIO) can reach 50-80%. It was estimated that the labeling efficiency for nanoscale iron oxides should be similar or higher than MPIO.

2.3. Biochemical Assays. *MTT Assay.* After treatment with nanoparticles, the replated neural cells were incubated with a 0.5 mg/mL MTT (Sigma) solution for an hour at 37 °C. The media and MTT were removed. The formazan crystals were dissolved in DMSO and centrifuged at 800 g for 5 min. The absorbance of the supernatants was measured at 490 nm on a microplate reader (BioRad Laboratories, Hercules, CA).

Live/Dead Assay. The cells were evaluated for viability using a Live/Dead staining kit (Molecular Probes, Eugene, OR) according to the manufacturer's instructions. After replating and incubation with nanoparticles, the spheroids were incubated in DMEM-F12 containing 3–10 μ M calcein-AM (green) and 8 μ M ethidium homodimer I (red) for 20 min at room temperature and protected from light according to the manufacturer's protocol. The cells were imaged under a fluorescent microscope (Olympus IX70, Melville, NY) or used for flow cytometry quantification.

Reactive Oxygen Species (ROS) Assay. Image-iT LIVE Green Reactive Oxygen Species Detection Kit (Molecular Probes I36007) was used to detect reactive oxygen species after exposure of spheroids to the magnetite nanoparticles. Briefly, a 25 μ M carboxy-H2DCFDA working solution was prepared from a 10 mM solution and used to label single cell suspensions after spheroid trypsinization. The cells were incubated in the dark for 30 min and then measured immediately using flow cytometry.

Iron Staining Assay. Iron Stain Kit (Prussian Blue Stain) (ab150674) was used to stain the magnetite nanoparticles. Briefly, the spheroids were washed with phosphate buffered saline (PBS) and stained with the working reagent made by mixing equal volumes of potassium ferricyanide and hydrochloric acid solutions according to the manufacturer's protocol. After 3 min, the spheroids were washed with PBS and counterstained with Nuclear Fast Red for 5 min. The wells were washed and images were taken under the microscope.

- 2.4. Immunohistochemistry. Immunohistochemistry was also done on replated spheroids for the Live/Dead assay and detection of neural degeneration biomarkers. Briefly, for the Live/Dead staining, the spheroids were incubated with calcein-AM and ethidium homodimer according to the manufacturer's protocol. Pictures were taken using a fluorescent microscope and images were analyzed using ImageJ software. For biomarker detection, the cells were fixed using 5% paraformaldehyde (PFA) and permeabilized using 0.2% Trixton-X 100. The samples were blocked with 5% fetal bovine serum (FBS) in PBS and stained with the primary antibodies for A β 42, tau, and p-tau, followed by the corresponding antispecies Alexa Fluoro antibodies (Alexa Fluor 488 goat antimouse IgG or Alexa Fluor 594 goat anti-Rabbit (Life technologies). Both primary and secondary antibody dilutions were made based on the manufacturer's recommendations and were prepared in staining buffer (2% FBS in PBS). The nuclei were then stained with Hoechst staining (blue), and pictures were taken for blue, green, and red colors to detect the markers and their cellular locations.
- 2.5. Flow Cytometry. After treatment with the corresponding nanoparticle size and concentration, replated spheroids were trypsinized. For the Live/Dead assay, the spheroids were treated with Calcein AM and ethedium homodimer after trypsinization (to get single cell suspension). For marker detection, trypsinized cells were fixed (5% PFA) and permeabilized with 100% cold methanol, blocked with 5% FBS in PBS, then stained with the corresponding marker antibody overnight. The secondary Alexa Fluor 488 or 586 antibody was later used, incubated for 1 h, removed and rinsed with PBS twice, and then taken for flow cytometry measurement. The cells were acquired with a BD FACSCanto II flow cytometer (Becton Dickinson, Franklin Lakes, NJ) and analyzed against isotype control using FlowJo software.
- **2.6.** Isolation of Extracellular Vesicles (EVs) and Nanoparticle Tracking Analysis. The conditioned EV-depleted media were collected from the cortical spheroid cultures of the control condition (no iron oxides), and the cultures exposed to 8, 15–20, and 20–30 nm iron oxides ($10~\mu M$). To isolate cortical spheroid-derived EVs, we performed the differential ultracentrifugation method followed by characterization using nanoparticle tracking analysis (NTA). Briefly, the conditioned media were centrifuged at 500 g for 5 min at 4 °C. The supernatants were collected and centrifuged again at 2000 g for 10 min. The collected supernatants were then centrifuged at 10~000~g for 30 min. Thereafter, an ultracentrifugation step was performed with supernatants at 100~000~g for 70 min. The EV-containing pellets were collected for subsequent experiments. Alternatively, EVs were isolated using an inexpensive polyethylene

glycol (PEG)-based method as reported previously. \$^{18,37}\$ Briefly, after centrifugation at 10 000 g for 30 min, supernatants were collected and mixed with PEG solution (16 wt %/vol in 1 M NaCl) at a 1:1 volume and incubated at 4 °C overnight. The mixed solutions were centrifuged at 3214 g for 1 h. The crude EV pellets were resuspended in PBS and then ultracentrifuged at 100 000 g for 70 min. Purified EV pellets were resuspended in 100 μ L of PBS. From our previous study, 18 the protein content of the isolated EVs was 2–3 μ g protein per mL spent medium.

Nanoparticle tracking analysis (NTA) was performed on the isolated EV samples in triplicate to determine size distribution and particle concentration. NTA was performed on a Nanosight LM10-HS instrument (Malvern Instruments, Malvern, UK) configured with a blue (488 nm) laser and sCMOS camera.³⁷ The EV samples were diluted to $1-2 \mu g$ protein per mL in PBS. For each replicate, three videos of 60 s were acquired with camera shutter speed fixed at 30.00 ms. To ensure accurate and consistent detection of small particles, camera level was set to 13, and detection threshold was maintained at three. The laser chamber was cleaned thoroughly with particle-free water and 70% ethanol between each sample reading. The collected videos were analyzed using NTA3.0 software to obtain the mode and mean size distribution, as well as the concentration of particles per mL of solution. Compared to the mean size, the mode size is usually a more accurate representation because the vesicle aggregates may affect the value of mean size.

- 2.7. Transmission Electron Microscopy. Electron microscopy imaging was performed to confirm the morphology of EVs according to Lasser et al.³⁸ and also as shown in our previous publication. Briefly, EV isolates were resuspended in 50–100 μ L of sterile filtered PBS. For each sample preparation, intact EVs (5 μ L) were dropped onto Parafilm. A carbon-coated 400 Hex mesh copper grid (Electron Microscopy Sciences, EMS) was positioned using forceps with coating side down on top of each drop for 1 h. Grids were washed with sterile filtered PBS three times and then the EV samples were fixed for 10 min in 2% PFA (EMS, EM grade). After washing, the grids were transferred on top of a 20 μ L drop of 2.5% glutaraldehyde (EMS, EM grade) and incubated for 10 min at room temperature. Grid samples were stained for 10 min with 2% uranyl acetate (EMS grade). Then the samples were embedded for 10 min with 0.13% methyl cellulose and 0.4% uranyl acetate. The coated side of the grids were left to dry before imaging on the CM120 Biotwin electron microscope.
- 2.8. Reverse Transcription Polymerase Chain Reaction (RT-PCR) Analysis. Total mRNA was isolated from different cell samples using the RNeasy Mini Kit (Qiagen, Valencia, CA) according to the manufacturer's protocol. The samples were further treated using DNA-Free RNA Kit (Zymo, Irvine, CA).³⁹ Reverse transcription was carried out according to the manufacturer's instructions using 2 $\mu\mathrm{g}$ of total mRNA, anchored oligo-dT primers (Operon, Huntsville, AL), and Superscript III (Invitrogen, Carlsbad, CA). The software Oligo Explorer 1.2 Primers (Genelink, Hawthorne, NY) was used to design the primers specific for target genes (Table S1). For normalization of expression levels, β -actin was used as an endogenous control. Using SYBR1 Green PCR Master Mix (Applied Biosystems), real-time RT-PCR reactions were performed on an ABI7500 instrument (Applied Biosystems, Foster City, CA), The amplification reactions were performed as follows: 2 min at 50 °C, 10 min at 95 °C, and 40 cycles at 95 °C for 15 s, 55 °C for 30 s, and 68 °C for 30 s. The Ct values of the target genes were first normalized to the Ct values of the endogenous control β -actin. The corrected Ct values were then compared for the treatment conditions to the experimental control. Fold changes in gene expression was calculated using the comparative Ct method: $2^{-(\Delta C_{\text{t treatment}} - \Delta C_{\text{t control}})}$ to obtain the relative expression
- **2.9. Magnetic Resonance Imaging (MRI) Analysis.** Sample Preparation. Iron-oxide-labeled cells were harvested with trypsin and then resuspended at 5×10^5 cells in a tissue-mimicking phantom made with agarose gel. Agarose cell layers were prepared by mixing an equal volume of cell suspension in media with a 2% (w/w) low-temperature agarose (VWR, Suwannee, GA) to form a solution at 1% (w/w) agarose-cell final concentration. As shown in our previous

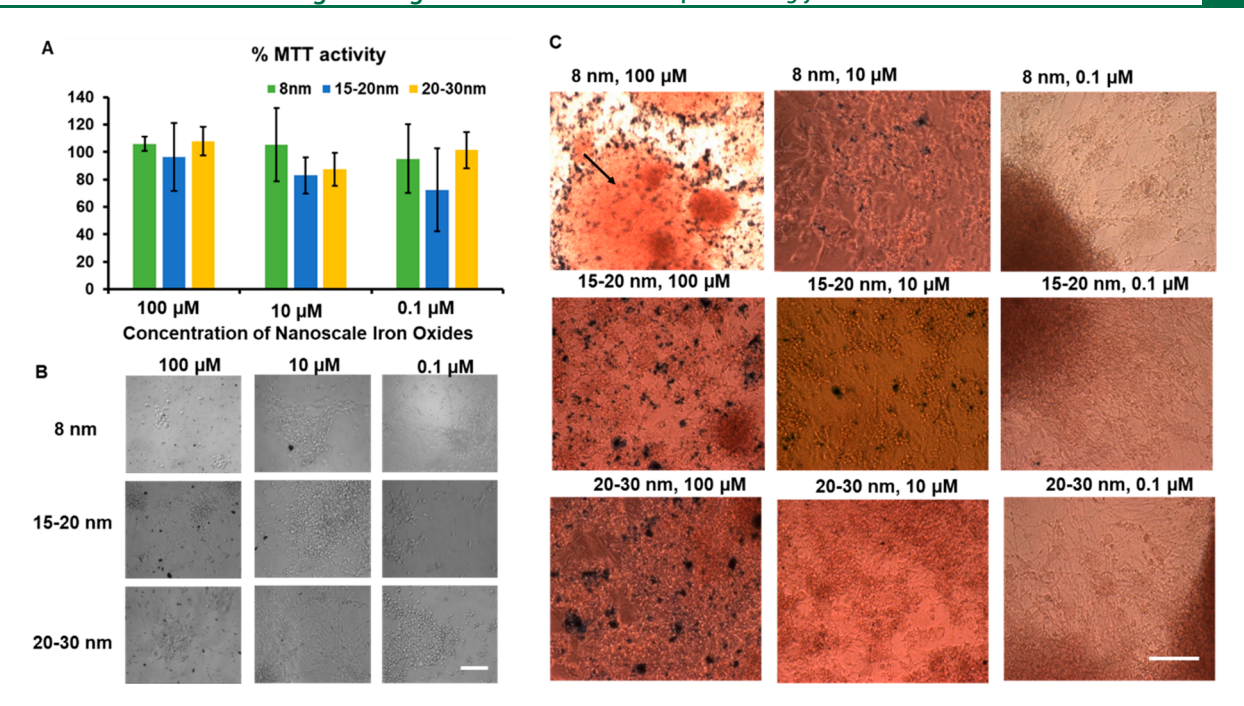


Figure 2. Metabolic characterizations of cortical spheroids after addition of iron oxide nanoparticles. Three concentrations were used in the cultures: 0.1 μ M (0.23 μ g Fe/mL), 10 μ M (2.34 μ g Fe/mL), and 100 μ M (23.4 μ g Fe/mL). (A) MTT activities of the cultures treated with different iron oxides of different sizes for 48 h (n=3). The % MTT activity is the relative absorbance of treated spheroids with nanoparticles compared to the untreated control. Statistical analysis showed no significant differences. (B) Morphology of replated cortical spheroids with different iron oxide nanoparticles. Scale bar: 100 μ m. (C) Iron staining images for replated cortical spheroids with different iron oxide nanoparticles. Arrow indicates the iron oxides inside the cortical spheroids. Scale bar: 100 μ m.

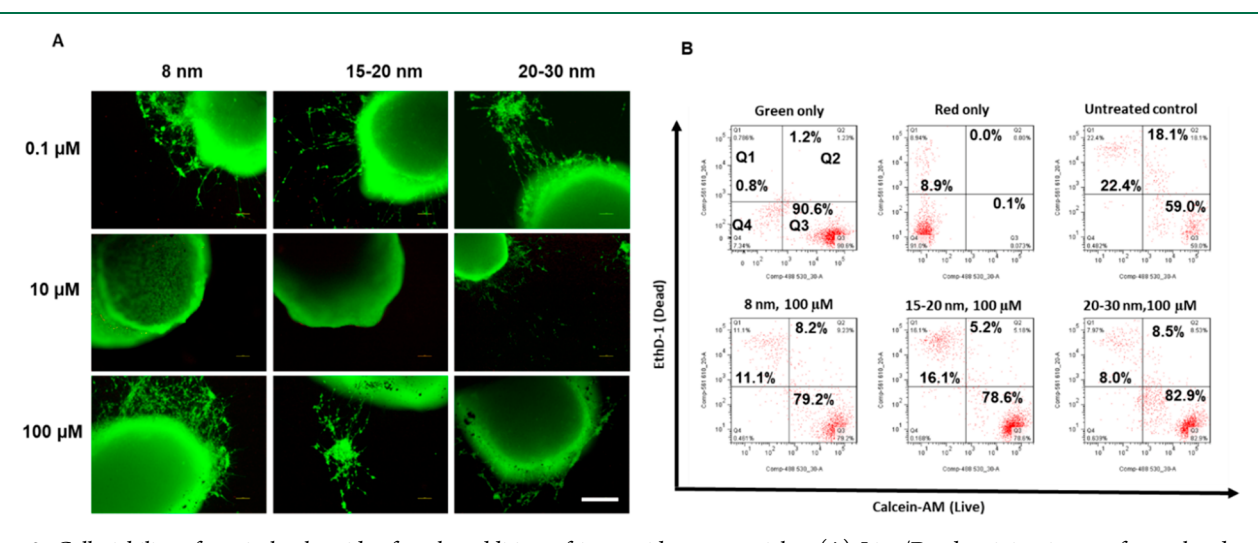


Figure 3. Cell viability of cortical spheroids after the addition of iron oxide nanoparticles. (A) Live/Dead staining images for replated cortical spheroids after addition of iron oxide nanoparticles for 48 h. Scale bar: $200 \, \mu \text{m}$. (B) Two-color flow cytometry dot plots for Live/Dead staining for the replated cortical spheroids after addition of iron oxide nanoparticles. The green only and red only controls indicate the proper color compensation.

studies, ^{35,36,40} the suspended cells were layered with a 1% agarose layer separating the cell-containing layers in a 10 mm NMR tube (Wilmad Glass, Buena, NJ). For all initial iron oxide exposures, the number of cells suspended in each layer was kept consistent

In Vitro MRI Experiments. Data were acquired using the 21.1-T, 900-MHz vertical magnet at the National High Magnetic Field Laboratory in Tallahassee, FL, USA. The magnet is equipped with a Bruker Avance III console using Paravision 5.1 (Resonance Research, Inc. Billerica, MA). A custom linear birdcage H radio frequency coil tunable to 900 MHz was used to evaluate EVs suspended in solution and cells dissociated from spheroids embedded in agarose gel. A 2D fast spin echo (FSE) sequence (TE = 11.34 ms, TR = 1.8 s) with 0.3 mm² in-plane resolution was used to assess the contrast of EVs

suspended in solution. To evaluate the cells, we used a 2D gradient recalled echo (GRE) sequence (TE = 2.5 ms, TR = 95 ms) with 0.1 mm 2 in-plane resolution as well as a 2D FSE sequence (TE = 11.34 ms, TR = 1.0 s) with 0.2 mm 2 in-plane resolution.

2.10. Statistical Analysis. The representative experiments were presented and the results were expressed as [mean ± standard deviation or mean ± standard error of the mean (SEM)]. To assess the statistical significance, one-way ANOVA or two-way ANOVA followed by Fisher's LSD post hoc tests were performed. A *p*-value <0.05 was considered statistically significant. For the two-way ANOVA, the two categories chosen were the nanoparticle size and the culture condition and the statistical analysis and graphs were generated using *Prism* 7.0 (https://prismsoftware.com).

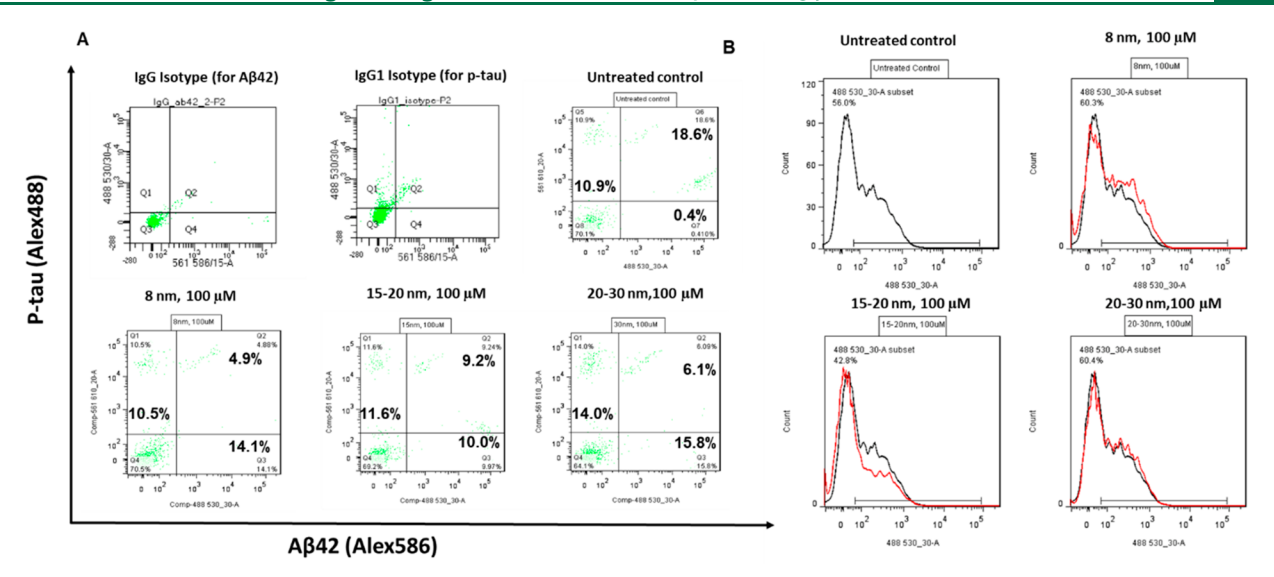


Figure 4. p-tau, $A\beta$ 42, and oxidative stress characterizations of cortical spheroids after addition of iron oxide nanoparticles. (A) Two-color flow cytometry dot plots for p-tau and $A\beta$ 42 expression for the replated cortical spheroids after addition of iron oxide nanoparticles for 48 h. (B) Flow cytometry analysis of reactive oxygen species for the replated cortical spheroids after addition of iron oxide nanoparticles for 48 h.

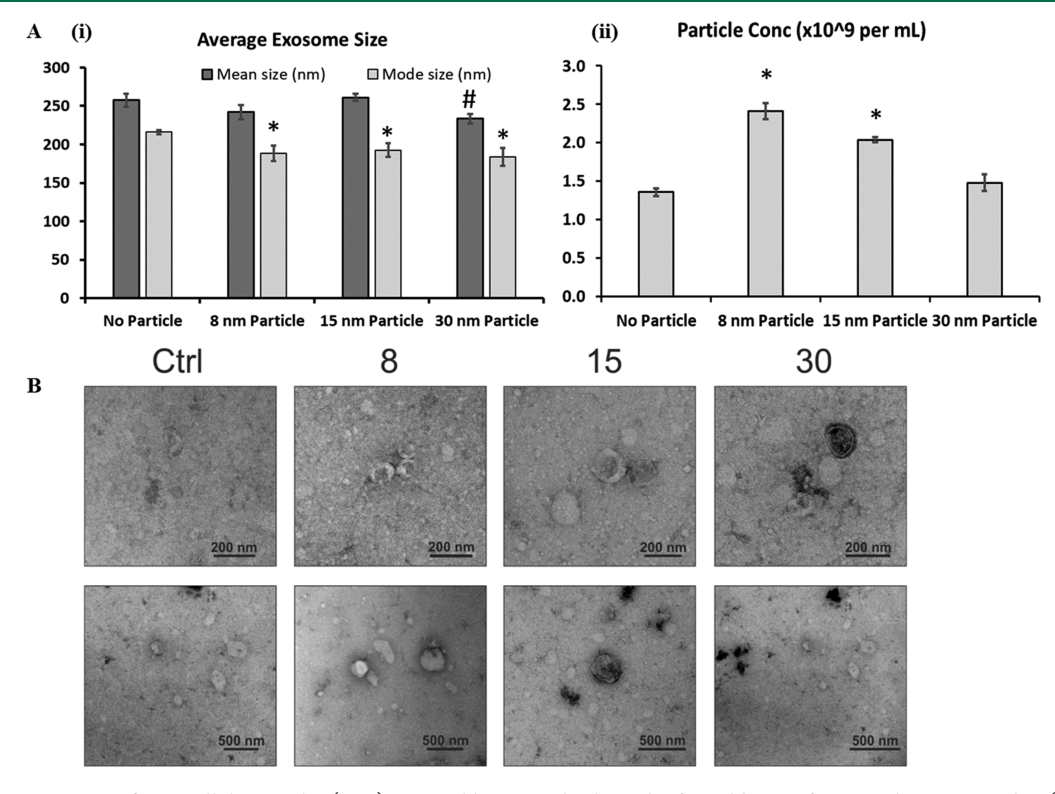


Figure 5. Characterizations of extracellular vesicles (EVs) secreted by cortical spheroids after addition of iron oxide nanoparticles. (A) Nanoparticle tracking analysis (NTA). (i) Mean and mode average particle size for isolated EVs. (ii) Particle concentration ($\times 10^9$ particles/mL). Particles were in 1 mL of particle-free phosphate buffer saline and originated from 6 mL of spent media. * and # indicate p < 0.05 compared to the control (n = 3). (B) Images of electron microscopy indicate the presence of exosome-sized, cup-shaped vesicles. Scale bar: 200 nm for the first panel and 500 nm for the second panel.

3. RESULTS

3.1. Characterizations of Cortical Spheroids after Addition of Iron Oxide Nanoparticles. The influence of iron oxide nanoparticles on the metabolic activities and the viability of cortical spheroids was evaluated using an MTT assay. Similar MTT activities were observed for cultures treated with three different sizes of iron oxides (8, 15–20, and 20–30 nm) at three different concentrations (0.1, 10, and 100

 μ M) (Figure 2A). The culture morphology of cortical spheroids outgrowth showed significant difference among different conditions (Figure 2B). Iron staining was performed to detect the iron oxides in the cultures treated with nanoparticles (Figure 2C). At high concentration of 100 μ M, iron oxide clusters were observed in the cultures as well as inside the cortical spheroids. However, at a low concentration of 0.1 μ M, the iron oxides were hardly observed. It is suspected

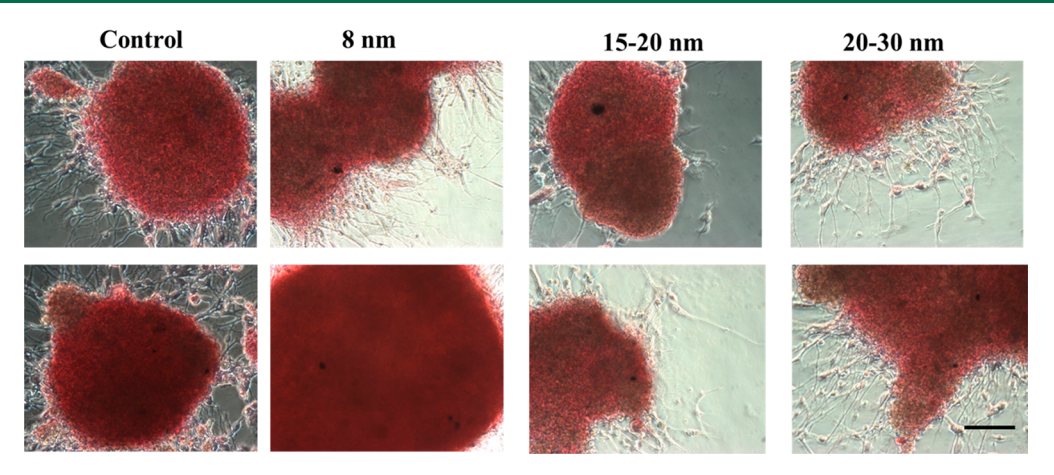


Figure 6. Indirect detection of iron oxides in isolated EVs from iron-oxide-labeled cortical spheroids by iron staining. Iron oxide nanoparticles (10 μ M) were added to a cortical spheroid culture, and EVs were isolated. The EVs were then added to another cortical spheroid cultures that were never exposed to iron oxides. Then iron staining was performed for the second culture. The brown color is the background. The black dots should be artifacts. Scale bar: 100 μ m.

that there is a higher incidence of aggregation and/or larger aggregates when iron oxide is at a higher concentration as compared to a lower concentration (0.1 μ M), and thus iron oxides were not observed at the lower concentration.

A Live/Dead assay was conducted after 24 h of treatment with iron oxide nanoparticles. The representative images are displayed in Figure 3A and no dead cells were observed based on the images. Then two-color flow cytometry was conducted after 48 h of incubation for the high concentration (100 μ M) condition (Figure 3B). The live cells (i.e., green cells in gate Q3) accounted for 78.6–82.9% of total cells, higher than the untreated control (59.0%), indicating that iron oxide nanoparticles did not have adverse effect on cell viability after 24–48 h of incubation (similar results were observed in the presence of A β 42 oligomers, as shown in Figure S1 and S2).

The expression of Alzheimer's disease markers p-tau and $A\beta$ 42 was examined after 48 h of incubation with the high concentration (100 μ M) iron oxide nanoparticles to check for neurodegeneration (Figure 4A). The results showed no obvious change in $A\beta$ 42 or p-tau expression. The ROS production was quantified using flow cytometry (Figure 4B). Similar expression of ROS was observed for the untreated control and the cultures incubated with high concentration (100 μ M) iron oxide nanoparticles. Taken together, these results indicate that iron oxide nanoparticles have no adverse effects on cell viability, metabolic activity, neurodegeneration, and oxidative stress.

3.2. Characterizations of Secreted Extracellular Vesicles after the Addition of Iron Oxides. The conditioned media from cortical spheroids incubated with different sizes of iron oxides were collected and the EVs were isolated. The NTA showed that the EV mean size was comparable for the no particle control vs 8 or 15 nm groups $(257.4 \pm 8.2 \text{ nm}, 242.0 \pm 9.5 \text{ nm}, \text{ and } 261.2 \pm 4.4 \text{ nm},$ respectively) (Figure 5A and Figure S3). However, the mean size of the 30 nm group (233.7 \pm 6.2 nm) was significantly smaller than that of the no-particle-treatment control. For mode size, the no-particle control (216.0 \pm 2.9 nm) was significantly larger than the three iron oxide groups (188.3 \pm 9.8 nm, 192.6 \pm 9.1 nm, and 183.9 \pm 11.6 nm, respectively). For EV particle concentration, the no-particle control was comparable to the 30 nm group $(1.36 \pm 0.05 \text{ vs } 1.48 \pm 0.11 \times$ 10⁹ per mL), which were both lower than those for the 8 and

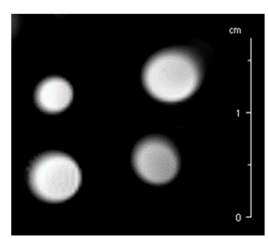
15 nm groups (2.41 \pm 0.10 or 2.04 \pm 0.04 \times 10⁹ per mL, respectively).

To further confirm the presence of exosomes, we analyzed preparations of different EV groups from cortical spheroid cultures labeled with different size of iron oxides by electron microscopy. In all samples, small round particles with typical cup-shaped morphology were observed, which indicates that exosomes were present (Figure 5B). However, no dark iron oxide nanoparticles could be observed inside the EVs. These results indicate effective isolation and confirmation of EVs/exosomes from cortical spheroids incubated with iron oxides.

3.3. Iron Oxides were Detected in the Labeled Cortical Spheroids but not in the EVs. To further investigate if the EVs contain iron oxides, the EVs isolated from cortical spheroids that have been incubated with iron oxides ($10~\mu M$) of different sizes were added to another cortical spheroid culture that was never exposed to iron oxides, and iron staining was performed (Figure 6). Despite the images' brown background, no iron oxides could be identified, which could be attributed to imaging technique, rather than the iron oxides not being packed as EV cargo. Thus, a better imaging method may be required to detect the nanoscale iron oxides.

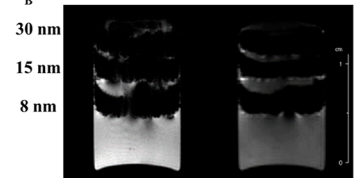
Then direct detection was performed by using MRI to examine the signal contrast generated from the iron-oxide nanoparticles (Figure 7). When suspended in solution, the EVs from iron-oxide-labeled cultures did not exhibit signal contrast compared to the control (i.e., EVs from the culture that was not exposed to iron oxides), indicating the lack of iron oxide nanoparticle (Figure 7A). MRI was also conducted on the dissociated cells from iron oxide-treated cortical spheroids layered in an agarose gel. Both GRE and FSE sequences generated high contrast images, indicating the presence of iron oxides in the cell (Figure 7B). However, quantitative measurements were not feasible due to the high level of contrast. These data indicate that during the EV biogenesis of iron-oxide-treated cortical spheroids the iron oxides were likely not packaged as EV cargo. Aggregation of iron oxide nanoparticles could be one of the contributing factors to this observation.

3.4. Characterizations of EV Biogenesis Markers. To examine the EV biogenesis in iron oxide-treated cortical



EV in solution. Clockwise from top left: 8 nm, control, 15-20 nm, 20-30 nm.

MRI of EV in solution utilizing a 2D Fast spin echo (FSE) sequence with TE = 11.34 ms, TR = 1.8 s and (0.3 mm)² in-plane resolution.



The left image was generated using a 2D Gradient Recalled Echo (GRE) sequence with TE = 2.5 ms, TR = 95

The right image was generated using a 2D FSE sequence with TE = 11.34 ms, TR = 1.0 s and (0.2 mm)² in-plane

Figure 7. MRI analysis of iron oxides in isolated EVs and dissociated cells from labeled cortical spheroids. (A) MRI analysis of EV samples. No contrast was observed. EV in solution: Clockwise from top left: 8 nm, control, 15-20 nm, 20-30 nm. MRI of EV in solution utilizing a 2D fast spin echo (FSE) sequence with TE = 11.34 ms, TR = 1.8 s, and $(0.3 \text{ mm})^2$ in-plane resolution. (B) MRI analysis of cells from iron-oxide-labeled cortical spheroids. The cells were layered in agarose gel. MRI of cells yielded high contrast. The left image was generated using a 2D Gradient Recalled Echo (GRE) sequence with TE = 2.5 ms, TR = 95 ms and $(0.1 \text{ mm})^2$ in-plane resolution. The right image was generated using a 2D FSE sequence with TE = 11.34 ms, TR = 1.0 s, and $(0.2 \text{ mm})^2$ in-plane resolution.

spheroids, we determined the expression of relevant markers⁴³ by RT-PCR for the cells that were either replated on Matrigelcoated surfaces or remained in suspension (Figure 8). The tested markers include CD63,44 CD81, Alix,45 TSG101, Syntenin-1,46 Syndecan, RAB27b,47 and ADAM10.5,48 Both the nanoparticle size and culture conditions had significant effects on the expressions of CD63, Alix, RAB27b, and Syndecan. On the other hand, the expression of CD81 and TSG101 were only significantly altered by the culture condition, whereas that of ADAM10 was only significantly affected by the nanoparticle size. For CD63, the 15 nm group had higher expression than the control (1.53 \pm 0.04 vs 0.95 \pm 0.03), whereas the 30 nm group (0.66 \pm 0.08) had slightly lower expression than the control. The suspension cultures (0.44-0.69) all had lower expression than the control. For CD81, the expression of the 8 nm group slightly decreased compared to the control (0.59 \pm 0.07 vs 0.89 \pm 0.07), while the 15 and 30 nm groups were comparable to the control. The suspension cultures (0.51-0.67) all had lower expression than the control. For Alix, the 15 nm group (1.92 ± 0.30) and 30 nm group (3.13 ± 0.41) had significantly higher expression than the control (0.81 \pm 0.11), whereas the remaining groups (0.61-1.32) had comparable expression. For TSG101, the replated nanoparticle groups (0.60-1.00) were comparable to the control group. The suspension control (1.16 \pm 0.04) and the 8 nm suspension group (1.19 ± 0.08) were slightly higher than the control (0.97 \pm 0.02), whereas the other suspension groups were similar to the control. For Syntenin-1, the 8 nm group (0.37 \pm 0.12) and 15 nm group (0.49 \pm 0.06) had lower expression than the control (0.87 ± 0.07) , whereas the remaining groups (0.73-0.89) had comparable expression to the control group.

For Syndecan, the 15 nm group (1.09 ± 0.08) and 30 nm group (1.07 ± 0.05) had slightly higher expression than the control (0.72 ± 0.14) . But the suspension 15 nm (0.34 ± 0.04) and 30 nm (0.27 ± 0.04) groups had lower expression than the control. For RAB27b, the 15 nm group (0.15 ± 0.05) was significantly lower than the control (0.89 ± 0.05) , while the 30 nm group (2.07 ± 0.14) was significantly higher. The

suspension 15 nm (0.52 \pm 0.07) and 30 nm groups (0.32 \pm 0.05) were lower than the control and the remaining groups were at a similar level to the control. For ADAM10, the 8 nm group (0.14 \pm 0.07) and suspension 30 nm group (0.08 \pm 0.04) had significantly lower expression compared to the control (0.75 \pm 0.16). The 30 nm group (7.31 \pm 0.73) and the suspension 8 nm group (11.51 \pm 4.61) had the significantly higher expression.

All together, these results indicate the differential expression of EV biogenesis markers in the iron-oxide-treated cultures compared to the no particle treatment control, and in suspension cultures compared to the adherent (i.e., replated) control.

4. DISCUSSION

Cytotoxicity is a major concern when using nanoparticles in vivo. 49 USPIOs have been the only medically approved nanoparticles and are useful because of their magnetic properties. However, studies have indicated that these particles may affect cells negatively by increasing ROS production, causing DNA damage and other complications. 50-53 The severity of cytotoxicity is dependent on the concentration and usually iron oxides are noncytotoxic under 100 μ g/mL.⁵⁴ Furthermore, the coating on the nanoparticles can affect the cytotoxicity. 52 Human tests involving USPIOs reported that patients had only minor symptoms and that degradation of iron oxides occurs through iron metabolic pathways.⁵⁴ One study with MCF-7 human breast cancer cell line shows that there is a decrease in cell viability and an increase of lactate dehydrogenase enzyme activity at high concentrations of iron oxide nanoparticles.⁵¹ In this study, no cytotoxicity and influence on metabolic activity, ROS, and neural degeneration was observed in cortical spheroids following the treatment with different sizes (8-30 nm) and concentration (up to 100 μ g/ mL) of iron oxides. Thus, labeling iPSC-derived cells with iron oxide nanoparticles under the conditions shown in this paper is safe and successful.

Stem-cell-derived EVs are known to be involved in paracrine actions in the body, helping stem cells communicate with damaged tissue for repair and recovery processes.² EVs can help restore tissues that were once thought to be unrepairable, such as the tissues of the central nervous system following a damage (e.g., stroke, spinal cord recovery). Although stem cells can be easily labeled with iron oxides, 35,36,55 EV labeling with iron oxides while retaining their integrity, structure, and morphology could be challenging. Some strategies involving the use of electroporation and sonication after EV isolation have been suggested; however, these mechanisms can damage the structure of EVs by creating pores in the lipid bilayer membrane and potentially alter their contents.²⁷ Introducing nanoscale iron oxides to stem cell cultures may invoke internalization and utilization of nanoparticles in EVs. 56,57 The study with adipose-derived stem cells (ASCs) has shown that these cells can uptake USPIOs at varying concentrations. Furthermore, USPIOs were confirmed in EVs by transmission electron microscopy and MRI,²⁷ which indicate that USPIO may be involved in the biogenesis of ASCs.

In this study, it is unclear for the reason and the potential mechanism by which 8 or 15 nm nanoparticles led to higher EV particle concentration based on nanoparticle tracking analysis. To answer this question, the cargo analysis of the EVs from different nanoparticle size group would need to be performed. It is suspected that the EV biogenesis pathway may

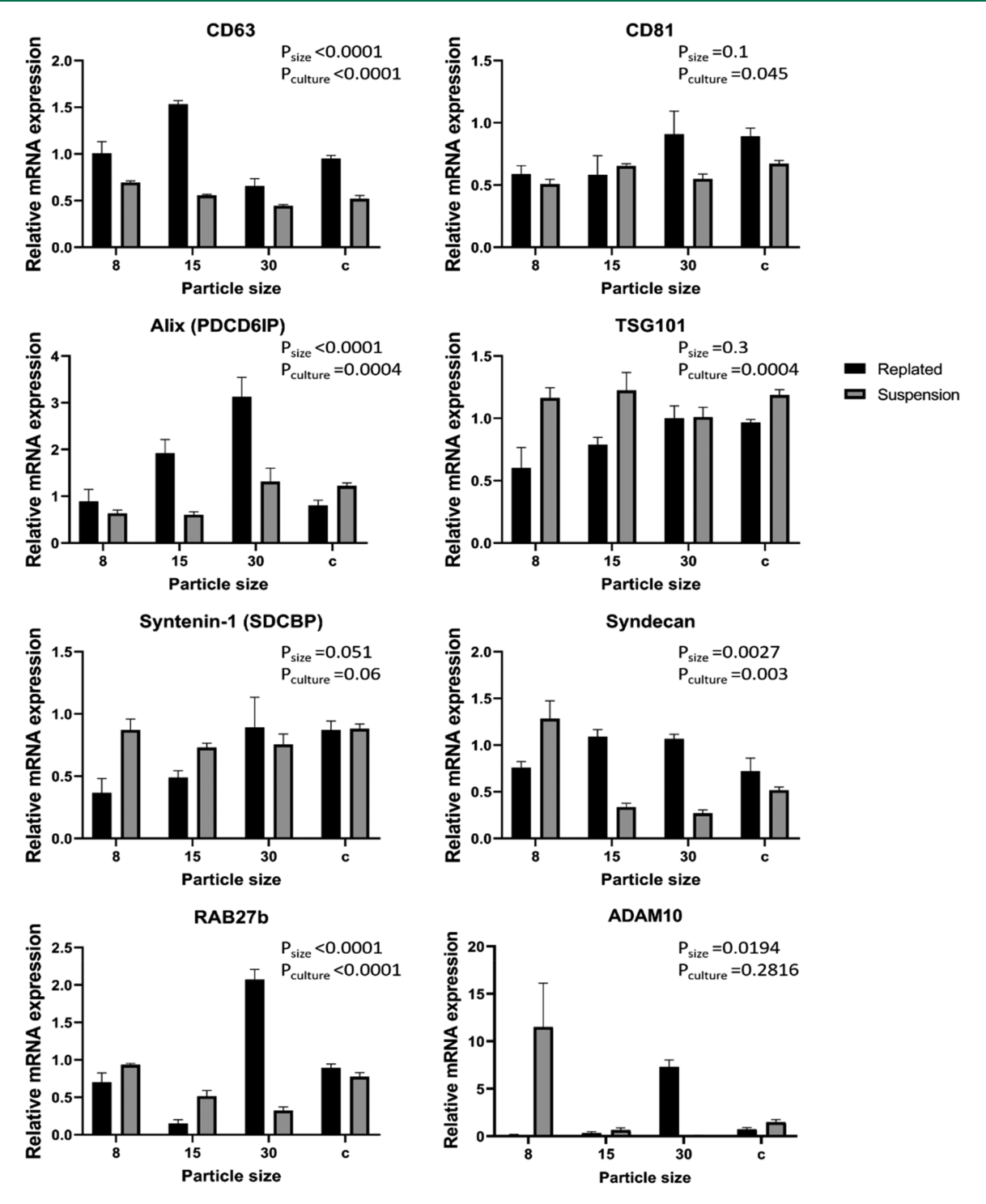


Figure 8. mRNA expression of EV biogenesis markers for replated or suspended cortical spheroids after the addition of iron oxide nanoparticles. The mRNA expression was normalized to one of the replicates of the control condition (i.e., replated cortical spheroids) (n = 3). Data are represented as mean \pm SEM and statistical analysis was done using a two-way ANOVA.

play a role in this process. In addition, iron oxide exposure was for a short-term of 2–4 days, thus it is not expected that the uptake of nanoparticles induces the differentiation of neural progenitor cells.^{35,36} Enhanced therapeutic effects of iron oxide-containing EVs have been reported.⁵⁶ The validation experiments and cargo analysis need to be performed when the labeling methods for the EVs are finalized in our future study.

In this study, no signal in the center of the cell layer was observed, which means that the contrast is too high to

effectively detect a signal from the tissue (Figure S2). However, because of the absence of detected cytotoxicity, altered metabolism, disrupted metabolism, and neurodegeneration, the iron oxides used in this study can be used for labeling the iPSC-derived cortical spheroids. The presence of iron oxides inside EVs could not be confirmed, which could be due to technical issues. The EV labeling can be improved by different ways: (i) designing a special iron oxide coating to enhance the internalization by EVs and the retention of

therapeutic molecules, ^{56,57} or (ii) reducing the iron oxide aggregation when adding to stem cell culture for indirect EV labeling. In addition, directly labeling EVs with iron oxides (or a different type of nanoparticles²⁴) after sonication or by transfection (e.g., electroporation) can eliminate the variations due to the culture conditions and EV biogenesis.

Other techniques involving different types of iron oxides or gold nanoparticles for EV labeling have been reported. 24,26 The iron oxides ranging from 5 nm to 20-30 nm in diameter have been reported to be internalized by mesenchymal stem-cellderived EVs. 56,57 Gold nanoparticles coated with glucose can be internalized into EVs via glucose transporter GLUT-1 and endocytic proteins.^{24,25} The mechanism is energy-dependent as the temperature at which the EVs are incubated with gold nanoparticles affects their internalization. EVs incubated at 37 °C were able to uptake significantly more glucose-coated gold nanoparticles (5 nm vs 20 nm) than those incubated at 4 °C.²⁴ One study used Gaussia luciferase and lactadherin and combined the two to form a fusion protein. Cells were transfected with this plasmid so that EVs would express this protein. Researchers found that the luminescent signal could not be seen in most organs 4 h postinjection,⁵⁸ which indicates that radioactive iodine-labeled EVs may give clearer insights on EV biodistribution.

EVs are known to contain different mRNAs that are highly important in paracrine processes as they can affect the gene expression in recipient cells.⁵ It has also been suggested that the geometry of the culture system can have an effect on uptake on nanoparticles and thus gene expression. 4,17,59 Here, this study sought to investigate the effects of the addition of nanoparticles to cortical spheroids in 2D and 3D cultures on the expression of EV trafficking and formation genes. Specifically, the relative expressions of CD63, Alix, Syntenin-1, TSG101 and others were tested. Our results show that the gene expression pertaining to EV synthesis is altered by iron oxide nanoparticle treatment, the size of the nanoparticles used, and by the culture condition (2D vs 3D). These results corroborate with previous studies showing that EV biogenesis may be affected by culture parameters, such as cell density, passage numbers, biophysical cues, 3D culture, and hypoxia. 4,59

5. CONCLUSIONS

This study investigated the effects of iron oxide nanoparticles on cortical spheroids derived from human iPSCs. Iron oxide nanoparticles do not induce significant cytotoxic effects to the cortical spheroids at varying concentrations that are below 100 μ M; therefore, they can be used for labeling human iPSCderived cells. The secreted extracellular vesicles were isolated and characterized, and exhibited characteristic exosome morphology. With uptake by dissociated cells and cultured organoids, iron oxide nanoparticles may influence the biogenesis of EVs when added to cortical spheroids in vitro but did not result in iron-oxide-labeled EVs. The mRNA expression of certain vesicle trafficking proteins including Alix, TSG101, ADAM10, CD63, Syntenin-1, and others was altered in nanoparticle cultures or suspension 3D cultures compared to adherent cultures. Analysis of the exosome content (e.g., using RNA-sequencing, microarray, or other functional assays) could give more insight into the functional role of these EVs and provide better understanding of gene expression. In addition, further investigations are needed to understand how much the contents of EVs are affected by

direct and indirect labeling methods and how the EV labeling may affect therapeutic properties.

ASSOCIATED CONTENT

Solution Supporting Information

The Supporting Information is available free of charge at https://pubs.acs.org/doi/10.1021/acsbiomaterials.0c01286.

Figure S1, flow cytometry analysis of live/dead cells after 48 h of incubation of replated neural spheroids with iron oxides in the presence of A β 42 oligomers; Figure S2, flow cytometry analysis of live/dead cells after 96 h of incubation of replated neural spheroids with iron oxides in the presence of A β 42 oligomers; Figure S3, examples of nanoparticle tracking analysis histogram for the extracellular vesicles secreted by iron-oxide-labeled cortical spheroids; Figure S4, MRI of an axial view of the gel within one of the cell layers; Table S1, primer sequence for target genes (PDF)

AUTHOR INFORMATION

Corresponding Author

Yan Li — Department of Chemical and Biomedical Engineering, Florida State University, Tallahassee, Florida 32306, United States; ⊙ orcid.org/0000-0002-5938-8519; Phone: 850-410-6320; Email: yli4@fsu.edu; Fax: 850-410-6150

Authors

- Mark Marzano Department of Chemical and Biomedical Engineering, Florida State University, Tallahassee, Florida 32306, United States
- Mayassa J. Bou-Dargham Department of Chemistry and Biochemistry, Florida State University, Tallahassee, Florida 32306, United States
- Allaura S. Cone Department of Biomedical Sciences, College of Medicine, Florida State University, Tallahassee, Florida 32304, United States
- Sara York Department of Biomedical Sciences, College of Medicine, Florida State University, Tallahassee, Florida 32304, United States
- Shannon Helsper Department of Chemical and Biomedical Engineering and The National High Magnetic Field Laboratory, Florida State University, Tallahassee, Florida 32306, United States
- Samuel C. Grant Department of Chemical and Biomedical Engineering and The National High Magnetic Field Laboratory, Florida State University, Tallahassee, Florida 32306, United States
- David G. Meckes, Jr. Department of Biomedical Sciences, College of Medicine, Florida State University, Tallahassee, Florida 32304, United States; orcid.org/0000-0002-0836-2108
- Qing-Xiang Amy Sang Department of Chemistry and Biochemistry, Florida State University, Tallahassee, Florida 32306, United States; orcid.org/0000-0001-8828-0569

Complete contact information is available at: https://pubs.acs.org/10.1021/acsbiomaterials.0c01286

Notes

The authors declare no competing financial interest.

ACKNOWLEDGMENTS

The authors thank Dr. Brian K. Washburn and Kristina Poduch at Florida State University's Department of Biological Sciences for their help with RT-PCR analysis and Ms. Ruth Didier at Florida State's Department of Biomedical Sciences for her help with flow cytometry. This work is partially supported by National Science Foundation (NSF, CAREER award, grant 1652992 to Y.L.) and the National Institutes of Health (NIH, USA) under Award R03NS102640 (to Y.L.). S.H. thanks the NIH for financial support through a Ruth Kirschstein National Research Service Award (F31NS115409). The content is solely the responsibility of the authors and does not necessarily represent the official views of the National Institutes of Health. A portion of this work was performed at the National High Magnetic Field Laboratory, which is supported by the NSF Cooperative Agreement No. DMR-1644779 and the State of Florida.

REFERENCES

- (1) Wiklander, O. P. B.; Brennan, M. A.; Lotvall, J.; Breakefield, X. O.; El Andaloussi, S. Advances in therapeutic applications of extracellular vesicles. *Sci. Transl. Med.* **2019**, *11* (492), eaav8521.
- (2) Riazifar, M.; Pone, E. J.; Lotvall, J.; Zhao, W. Stem Cell Extracellular Vesicles: Extended Messages of Regeneration. *Annu. Rev. Pharmacol. Toxicol.* **2017**, *57*, 125–154.
- (3) Adamiak, M.; Cheng, G.; Bobis-Wozowicz, S.; Zhao, L.; Kedracka-Krok, S.; Samanta, A.; Karnas, E.; Xuan, Y. T.; Skupien-Rabian, B.; Chen, X.; Jankowska, U.; Girgis, M.; Sekula, M.; Davani, A.; Lasota, S.; Vincent, R. J.; Sarna, M.; Newell, K. L.; Wang, O. L.; Dudley, N.; Madeja, Z.; Dawn, B.; Zuba-Surma, E. K. Induced Pluripotent Stem Cell (iPSC)-Derived Extracellular Vesicles Are Safer and More Effective for Cardiac Repair Than iPSCs. Circ. Res. 2018, 122 (2), 296–309.
- (4) Jeske, R.; Bejoy, J.; Marzano, M.; Li, Y. Human induced pluripotent stem cell-derived extracellular vesicles: characteristics and applications. *Tissue Eng., Part B* **2020**, *26* (2), 129–144.
- (5) Colombo, M.; Raposo, G.; Thery, C. Biogenesis, secretion, and intercellular interactions of exosomes and other extracellular vesicles. *Annu. Rev. Cell Dev. Biol.* **2014**, *30*, 255–89.
- (6) Jung, J. H.; Fu, X.; Yang, P. C. Exosomes Generated From iPSC-Derivatives: New Direction for Stem Cell Therapy in Human Heart Diseases. *Circ. Res.* **2017**, *120* (2), 407–417.
- (7) Khan, M.; Nickoloff, E.; Abramova, T.; Johnson, J.; Verma, S. K.; Krishnamurthy, P.; Mackie, A. R.; Vaughan, E.; Garikipati, V. N.; Benedict, C.; Ramirez, V.; Lambers, E.; Ito, A.; Gao, E.; Misener, S.; Luongo, T.; Elrod, J.; Qin, G.; Houser, S. R.; Koch, W. J.; Kishore, R. Embryonic stem cell-derived exosomes promote endogenous repair mechanisms and enhance cardiac function following myocardial infarction. *Circ. Res.* **2015**, *117* (1), 52–64.
- (8) Liu, B.; Lee, B. W.; Nakanishi, K.; Villasante, A.; Williamson, R.; Metz, J.; Kim, J.; Kanai, M.; Bi, L.; Brown, K.; Di Paolo, G.; Homma, S.; Sims, P. A.; Topkara, V. K.; Vunjak-Novakovic, G. Cardiac recovery via extended cell-free delivery of extracellular vesicles secreted by cardiomyocytes derived from induced pluripotent stem cells. *Nat. Biomed Eng.* **2018**, 2 (5), 293–303.
- (9) Webb, R. L.; Kaiser, E. E.; Jurgielewicz, B. J.; Spellicy, S.; Scoville, S. L.; Thompson, T. A.; Swetenburg, R. L.; Hess, D. C.; West, F. D.; Stice, S. L. Human Neural Stem Cell Extracellular Vesicles Improve Recovery in a Porcine Model of Ischemic Stroke. Stroke 2018, 49 (5), 1248–1256.
- (10) Webb, R. L.; Kaiser, E. E.; Scoville, S. L.; Thompson, T. A.; Fatima, S.; Pandya, C.; Sriram, K.; Swetenburg, R. L.; Vaibhav, K.; Arbab, A. S.; Baban, B.; Dhandapani, K. M.; Hess, D. C.; Hoda, M. N.; Stice, S. L. Human Neural Stem Cell Extracellular Vesicles Improve Tissue and Functional Recovery in the Murine Thromboembolic Stroke Model. *Transl. Stroke Res.* **2018**, *9* (5), 530–539.

- (11) Povero, D.; Pinatel, E. M.; Leszczynska, A.; Goyal, N. P.; Nishio, T.; Kim, J.; Kneiber, D.; de Araujo Horcel, L.; Eguchi, A.; Ordonez, P. M.; Kisseleva, T.; Feldstein, A. E. Human induced pluripotent stem cell-derived extracellular vesicles reduce hepatic stellate cell activation and liver fibrosis. *JCI Insight* **2019**, *4*, e125642.
- (12) Liu, S.; Mahairaki, V.; Bai, H.; Ding, Z.; Li, J.; Witwer, K. W.; Cheng, L. Highly Purified Human Extracellular Vesicles Produced by Stem Cells Alleviate Aging Cellular Phenotypes of Senescent Human Cells. *Stem Cells* **2019**, *37*, 779–790.
- (13) Ding, Q.; Sun, R.; Wang, P.; Zhang, H.; Xiang, M.; Meng, D.; Sun, N.; Chen, A. F.; Chen, S. Protective effects of human induced pluripotent stem cell-derived exosomes on high glucose-induced injury in human endothelial cells. *Exp. Ther. Med.* **2018**, *15* (6), 4791–4797.
- (14) Kim, S.; Lee, S. K.; Kim, H.; Kim, T. M. Exosomes Secreted from Induced Pluripotent Stem Cell-Derived Mesenchymal Stem Cells Accelerate Skin Cell Proliferation. *Int. J. Mol. Sci.* **2018**, *19* (10), 3119
- (15) Podvin, S.; Jones, A.; Liu, Q.; Aulston, B.; Ransom, L. S.; Ames, J.; Shen, G.; Lietz, C. B.; Jiang, Z.; O'Donoghue, A. J.; Winston, C.; Ikezu, T.; Rissman, R.; Yuan, S.; Hook, V. Dysregulation of Exosome Cargo by Mutant Tau Expressed in Human-Induced Pluripotent Stem Cell (iPSC) Neurons Revealed by Proteomics Analyses. *Mol. Cell Proteomics* 2020, 19, 1017.
- (16) Eguchi, T.; Sogawa, C.; Okusha, Y.; Uchibe, K.; Iinuma, R.; Ono, K.; Nakano, K.; Murakami, J.; Itoh, M.; Arai, K.; Fujiwara, T.; Namba, Y.; Murata, Y.; Ohyama, K.; Shimomura, M.; Okamura, H.; Takigawa, M.; Nakatsura, T.; Kozaki, K. I.; Okamoto, K.; Calderwood, S. K. Organoids with cancer stem cell-like properties secrete exosomes and HSP90 in a 3D nanoenvironment. *PLoS One* **2018**, *13* (2), e0191109.
- (17) Villasante, A.; Marturano-Kruik, A.; Ambati, S. R.; Liu, Z.; Godier-Furnemont, A.; Parsa, H.; Lee, B. W.; Moore, M. A.; Vunjak-Novakovic, G. Recapitulating the Size and Cargo of Tumor Exosomes in a Tissue-Engineered Model. *Theranostics* **2016**, *6* (8), 1119–30.
- (18) Marzano, M.; Bejoy, J.; Cheerathodi, M.; Sun, L.; York, S.; Zhao, J.; Kanekiyo, T.; Bu, G.; Meckes, D. G., Jr.; Li, Y. Differential effects of extracellular vesicles of lineage-specific human pluripotent stem cells on cellular behaviours of isogenic cortical spheroids. *Cells* **2019**, *8*, 993–1014.
- (19) Pasca, S. P. The rise of three-dimensional human brain cultures. *Nature* **2018**, 553 (7689), 437–445.
- (20) Kelava, I.; Lancaster, M. A. Stem cell models of human brain development. *Cell Stem Cell* **2016**, *18* (6), 736–748.
- (21) Lancaster, M. A.; Renner, M.; Martin, C. A.; Wenzel, D.; Bicknell, L. S.; Hurles, M. E.; Homfray, T.; Penninger, J. M.; Jackson, A. P.; Knoblich, J. A. Cerebral organoids model human brain development and microcephaly. *Nature* **2013**, *501* (7467), 373–9.
- (22) Song, L.; Yuan, X.; Jones, Z.; Griffin, K.; Zhou, Y.; Ma, T.; Li, Y. Assembly of human stem cell-derived cortical spheroids and vascular spheroids to model 3-D brain-like tissues. *Sci. Rep.* **2019**, *9*, 5977.
- (23) Song, L.; Yuan, X.; Jones, Z.; Vied, C.; Miao, Y.; Marzano, M.; Hua, T.; Sang, Q. X.; Guan, J.; Ma, T.; Zhou, Y.; Li, Y. Functionalization of Brain Region-specific Spheroids with Isogenic Microglia-like Cells. *Sci. Rep.* **2019**, *9*, 11055–11072.
- (24) Betzer, O.; Perets, N.; Angel, A.; Motiei, M.; Sadan, T.; Yadid, G.; Offen, D.; Popovtzer, R. In Vivo Neuroimaging of Exosomes Using Gold Nanoparticles. ACS Nano 2017, 11 (11), 10883–10893.
- (25) Perets, N.; Betzer, O.; Shapira, R.; Brenstein, S.; Angel, A.; Sadan, T.; Ashery, U.; Popovtzer, R.; Offen, D. Golden Exosomes Selectively Target Brain Pathologies in Neurodegenerative and Neurodevelopmental Disorders. *Nano Lett.* **2019**, *19*, 3422–3431.
- (26) Islam, M. K.; Syed, P.; Lehtinen, L.; Leivo, J.; Gidwani, K.; Wittfooth, S.; Pettersson, K.; Lamminmaki, U. A Nanoparticle-Based Approach for the Detection of Extracellular Vesicles. *Sci. Rep.* **2019**, 9 (1), 10038.
- (27) Busato, A.; Bonafede, R.; Bontempi, P.; Scambi, I.; Schiaffino, L.; Benati, D.; Malatesta, M.; Sbarbati, A.; Marzola, P.; Mariotti, R.

- Magnetic resonance imaging of ultrasmall superparamagnetic iron oxide-labeled exosomes from stem cells: a new method to obtain labeled exosomes. *Int. J. Nanomed.* **2016**, *11*, 2481–90.
- (28) Wang, Y.; Liu, Z.; Wang, X.; Dai, Y.; Li, X.; Gao, S.; Yu, P.; Lin, Q.; Fan, Z.; Ping, Y.; Wang, D.; Lin, X.; Zheng, Z.; Liu, W.; Tao, Z. Rapid and Quantitative Analysis of Exosomes by a Chemiluminescence Immunoassay Using Superparamagnetic Iron Oxide Particles. *J. Biomed. Nanotechnol.* **2019**, *15* (8), 1792–1800.
- (29) Zhang, K.; Zhao, X.; Chen, X.; Wei, Y.; Du, W.; Wang, Y.; Liu, L.; Zhao, W.; Han, Z.; Kong, D.; Zhao, Q.; Guo, Z.; Han, Z.; Liu, N.; Ma, F.; Li, Z. Enhanced Therapeutic Effects of Mesenchymal Stem Cell-Derived Exosomes with an Injectable Hydrogel for Hindlimb Ischemia Treatment. ACS Appl. Mater. Interfaces 2018, 10 (36), 30081–30091.
- (30) Du, W.; Zhang, K.; Zhang, S.; Wang, R.; Nie, Y.; Tao, H.; Han, Z.; Liang, L.; Wang, D.; Liu, J.; Liu, N.; Han, Z.; Kong, D.; Zhao, Q.; Li, Z. Enhanced proangiogenic potential of mesenchymal stem cell-derived exosomes stimulated by a nitric oxide releasing polymer. *Biomaterials* **2017**, 133, 70–81.
- (31) Quijano, L. M.; Naranjo, J. D.; El-Mossier, S.; Turner, N. J.; Pineda Molina, C.; Bartolacci, J.; Zhang, L.; White, L.; Li, H.; Badylak, S. F. Matrix-Bound Nanovesicles: The Effects of Isolation Method Upon Yield, Purity and Function. *Tissue Eng., Part C* **2020**, 26, 528.
- (32) Huleihel, L.; Hussey, G. S.; Naranjo, J. D.; Zhang, L.; Dziki, J. L.; Turner, N. J.; Stolz, D. B.; Badylak, S. F. Matrix-bound nanovesicles within ECM bioscaffolds. *Sci. Adv.* **2016**, 2 (6), e1600502.
- (33) Yan, Y.; Bejoy, J.; Xia, J.; Guan, J.; Zhou, Y.; Li, Y. Neural patterning of human induced pluripotent stem cells in 3-D cultures for studying biomolecule-directed differential cellular responses. *Acta Biomater.* **2016**, 42, 114–126.
- (34) Yan, Y.; Song, L.; Madinya, J.; Ma, T.; Li, Y. Derivation of cortical spheroids from human induced pluripotent stem cells in a suspension bioreactor. *Tissue Eng., Part A* **2018**, 24 (5–6), 418–431.
- (35) Sart, S.; Calixto Bejarano, F.; Baird, M. A.; Yan, Y.; Rosenberg, J. T.; Ma, T.; Grant, S. C.; Li, Y. Intracellular labeling of mouse embryonic stem cell-derived neural progenitor aggregates with micron-sized particles of iron oxide. *Cytotherapy* **2015**, *17* (1), 98–111.
- (36) Yan, Y.; Calixto Bejarano, F.; Sart, S.; Muroski, M.; Strouse, G. F.; Grant, S. C.; Li, Y. Cryopreservation of embryonic stem cell-derived multicellular neural aggregates labeled with micron-sized particles of iron oxide for magnetic resonance imaging. *Biotechnol. Prog.* **2015**, *31* (2), 510–521.
- (37) Rider, M. A.; Hurwitz, S. N.; Meckes, D. G., Jr. ExtraPEG: A Polyethylene Glycol-Based Method for Enrichment of Extracellular Vesicles. *Sci. Rep.* **2016**, *6*, 23978.
- (38) Lasser, C.; Eldh, M.; Lotvall, J. Isolation and characterization of RNA-containing exosomes. *J. Visualized Exp.* **2012**, *59*, e3037.
- (39) Song, L.; Wang, K.; Li, Y.; Yang, Y. Nanotopography promoted neuronal differentiation of human induced pluripotent stem cells. *Colloids Surf., B* **2016**, *148*, 49–58.
- (40) Rosenberg, J. T.; Sachi-Kocher, A.; Davidson, M. W.; Grant, S. C. Intracellular SPIO labeling of microglia: high field considerations and limitations for MR microscopy. *Contrast Media Mol. Imaging* **2012**, 7 (2), 121–9.
- (41) Fu, R.; Brey, W. W.; Shetty, K.; Gor'kov, P.; Saha, S.; Long, J. R.; Grant, S. C.; Chekmenev, E. Y.; Hu, J.; Gan, Z.; Sharma, M.; Zhang, F.; Logan, T. M.; Bruschweller, R.; Edison, A.; Blue, A.; Dixon, I. R.; Markiewicz, W. D.; Cross, T. A. Ultra-wide bore 900 MHz high-resolution NMR at the National High Magnetic Field Laboratory. *J. Magn. Reson.* **2005**, *177* (1), 1–8.
- (42) Lo Cicero, A.; Stahl, P. D.; Raposo, G. Extracellular vesicles shuffling intercellular messages: for good or for bad. *Curr. Opin. Cell Biol.* **2015**, 35, 69–77.
- (43) Kowal, J.; Arras, G.; Colombo, M.; Jouve, M.; Morath, J. P.; Primdal-Bengtson, B.; Dingli, F.; Loew, D.; Tkach, M.; Thery, C. Proteomic comparison defines novel markers to characterize

- heterogeneous populations of extracellular vesicle subtypes. *Proc. Natl. Acad. Sci. U. S. A.* **2016**, *113* (8), E968–77.
- (44) Hurwitz, S. N.; Cheerathodi, M. R.; Nkosi, D.; York, S. B.; Meckes, D. G. Tetraspanin CD63 Bridges Autophagic and Endosomal Processes To Regulate Exosomal Secretion and Intracellular Signaling of Epstein-Barr Virus LMP1. *J. Virol.* **2018**, *92* (5), e01969.
- (45) Sun, R.; Liu, Y.; Lu, M.; Ding, Q.; Wang, P.; Zhang, H.; Tian, X.; Lu, P.; Meng, D.; Sun, N.; Xiang, M.; Chen, S. ALIX increases protein content and protective function of iPSC-derived exosomes. *J. Mol. Med.* (*Heidelberg, Ger.*) **2019**, 97, 829–844.
- (46) Cone, A. S.; Hurwitz, S. N.; Lee, G.; Yuan, X.; Zhou, Y.; Li, Y.; Meckes, D. G., Jr. Alix and Syntenin-1 traffic amyloid precursor protein into extracellular vesicles. *BMC Molecular and Cell Biology* **2020**, *21*, 58–78.
- (47) Ostrowski, M.; Carmo, N. B.; Krumeich, S.; Fanget, I.; Raposo, G.; Savina, A.; Moita, C. F.; Schauer, K.; Hume, A. N.; Freitas, R. P.; Goud, B.; Benaroch, P.; Hacohen, N.; Fukuda, M.; Desnos, C.; Seabra, M. C.; Darchen, F.; Amigorena, S.; Moita, L. F.; Thery, C. Rab27a and Rab27b control different steps of the exosome secretion pathway. *Nat. Cell Biol.* **2010**, *12* (1), 19–30.
- (48) Stuffers, S.; Sem Wegner, C.; Stenmark, H.; Brech, A. Multivesicular endosome biogenesis in the absence of ESCRTs. *Traffic* **2009**, *10* (7), 925–37.
- (49) Soenen, S. J.; De Cuyper, M. How to assess cytotoxicity of (iron oxide-based) nanoparticles: a technical note using cationic magnetoliposomes. *Contrast Media Mol. Imaging* **2011**, *6* (3), 153–64.
- (50) Guichard, Y.; Schmit, J.; Darne, C.; Gate, L.; Goutet, M.; Rousset, D.; Rastoix, O.; Wrobel, R.; Witschger, O.; Martin, A.; Fierro, V.; Binet, S. Cytotoxicity and genotoxicity of nanosized and microsized titanium dioxide and iron oxide particles in Syrian hamster embryo cells. *Ann. Occup. Hyg.* **2012**, *56* (5), 631–644.
- (51) Alarifi, S.; Ali, D.; Alkahtani, S.; Alhader, M. S. Iron oxide nanoparticles induce oxidative stress, DNA damage, and caspase activation in the human breast cancer cell line. *Biol. Trace Elem. Res.* **2014**, *159* (1–3), 416–24.
- (52) Soenen, S. J.; Himmelreich, U.; Nuytten, N.; De Cuyper, M. Cytotoxic effects of iron oxide nanoparticles and implications for safety in cell labelling. *Biomaterials* **2011**, 32 (1), 195–205.
- (53) Soenen, S. J.; Nuytten, N.; De Meyer, S. F.; De Smedt, S. C.; De Cuyper, M. High intracellular iron oxide nanoparticle concentrations affect cellular cytoskeleton and focal adhesion kinase-mediated signaling. *Small* **2010**, *6* (7), 832–42.
- (54) Singh, N.; Jenkins, G. J.; Asadi, R.; Doak, S. H. Potential toxicity of superparamagnetic iron oxide nanoparticles (SPION). *Nano Rev.* **2010**, *1*, 5358.
- (55) Rosenberg, J. T.; Sellgren, K. L.; Sachi-Kocher, A.; Calixto Bejarano, F.; Baird, M. A.; Davidson, M. W.; Ma, T.; Grant, S. C. Magnetic resonance contrast and biological effects of intracellular superparamagnetic iron oxides on human mesenchymal stem cells with long-term culture and hypoxic exposure. *Cytotherapy* **2013**, *15* (3), 307–22.
- (56) Lee, J. R.; Park, B. W.; Kim, J.; Choo, Y. W.; Kim, H. Y.; Yoon, J. K.; Kim, H.; Hwang, J. W.; Kang, M.; Kwon, S. P.; Song, S. Y.; Ko, I. O.; Park, J. A.; Ban, K.; Hyeon, T.; Park, H. J.; Kim, B. S. Nanovesicles derived from iron oxide nanoparticles-incorporated mesenchymal stem cells for cardiac repair. *Sci. Adv.* 2020, 6 (18), eaaz0952.
- (57) Kim, H. Y.; Kim, T. J.; Kang, L.; Kim, Y. J.; Kang, M. K.; Kim, J.; Ryu, J. H.; Hyeon, T.; Yoon, B. W.; Ko, S. B.; Kim, B. S. Mesenchymal stem cell-derived magnetic extracellular nanovesicles for targeting and treatment of ischemic stroke. *Biomaterials* **2020**, 243, 119942.
- (58) Morishita, M.; Takahashi, Y.; Nishikawa, M.; Sano, K.; Kato, K.; Yamashita, T.; Imai, T.; Saji, H.; Takakura, Y. Quantitative analysis of tissue distribution of the B16BL6-derived exosomes using a streptavidin-lactadherin fusion protein and iodine-125-labeled biotin derivative after intravenous injection in mice. *J. Pharm. Sci.* **2015**, *104* (2), 705–13.
- (59) Patel, D. B.; Santoro, M.; Born, L. J.; Fisher, J. P.; Jay, S. M. Towards rationally designed biomanufacturing of therapeutic

extracellular vesicles: impact of the bioproduction microenvironment. Biotechnol. Adv. $2018,\ 36\ (8),\ 2051-2059.$